AKARI/IRC All-Sky Survey Bright Source Catalogue Version $\beta - 1$
– Release Note (Rev.1) –

AKARI/IRC Team
Prepared by H. Kataza [1], C. Alfageme [2], A. Cassatella [2], N. Cox [2],
H. Fujiwara [3], D. Ishihara [4], S. Oyabu [1], A. Salama [2], S. Takita [1],
I. Yamamura [1]

November 17, 2009

Abstract

The AKARI/IRC Point Source Catalogue Version β-1 provides positions and fluxes of 877,091 sources (851,189 sources in 9μm band and 195,893 sources in 18μm band) in the Mid-Infrared wavelengths. This document describes the outline of the data processing and calibration, and basic performance of the released catalogue. As the current version is the first preliminary version, the users of the catalogue are requested to read this document carefully before critical discussions with the data.

IMPORTANT: Sources in this release must be referred to in the literatures as AKARI-IRC-b1 J0123456+776543, where b1 indicates the release version.

Any questions and comments are appreciated via ISAS Helpdesk *iris_help@ir.isas.jaxa.jp*.

Release history		
2009/11/17	Rev.1	Release

Contents

---

[1] ISAS/JAXA
[2] ESAC/ESA
[3] Tokyo Univ.
[4] Nagoya Univ.

1 Overview

1.1 The AKARI All-Sky Survey

The Infrared Astronomical Satellite AKARI (Murakami et al. 2007) was launched on February 21st, 2006 (UT). After three weeks of performance verification phase (PV) (April 13th to May 7th), Phase 1 observation started on the May 8th and continued until November 9th, followed by Phase 2 observation until the exhaustion of liquid Helium on the August 26th, 2007. One of the main missions of AKARI is to carry out the All-Sky Survey in four photometric bands in the far-infrared wavelengths in 50μm -180μm range with the Far-Infrared Surveyor (FIS; Kawada et al. 2007), and in two mid-infrared bands with effective wavelength at 9 and 18 μm with the Infrared Camera (IRC; Onaka et al. 2007). The All-Sky Survey had the highest priority in Phase 1 operations. In Phase 2 the observation plan was highly optimized for the FIS survey (not for the IRC survey) to fill the scan gaps caused in Phase 1 under constraints of carrying out the maximum number of pointed observations. As the result the IRC scanned TBD [5] percent of the entire sky twice or more in the 16 months of the cryogenic mission phase.

The primary product from the survey is the point source catalogue that we describe in this document. It is regarded as the primary catalogue from the AKARI IRC survey. The catalogue is supposed to have a uniform detection limit over the entire sky, based on the uniform source detection limit per scan observation. Redundant observations are used to increase the reliability of the detection.

1.2 The Infrared Camera All-Sky Survey

The Infrared Camera All-Sky Survey has been done by two channel of the Infrared Camera (IRC): MIR-S channel and MIR-L channel. The specifications of the two channels are summarized in Table1. MIR-L has a field of view at about 20 arcminutes away from that of MIR-S. Photometric bands used for the All-Sky Survey are S9W (6.7 – 11.6 μm; MIR-S) with the effective wavelength at 9 μm and L18W (13.9 – 25.6 μm; MIR-L) with the effective wavelength at 18 μm. Figure 1 shows the relative spectral response (link to the data exists in "AKARI Observers Page" *http://www.ir.isas.jaxa.jp/ASTRO-F/Observation/*, see also AKARI IRC Data User Manual v1.4) for both bands.

Table 1: IRC MIR-L and MIR-S Specification

	MIR-S	MIR-L
Camera Field of View (arcmin)	$10' \times 9'.6$	$10'.7 \times 10'.2$
Pixel scale (arcsec)	$2''.34 \times 2''.34$	$2''.51 \times 2''.39$
Band for All-Sky Survey	S9W	L18W
Effective wavelength	9μm	18μm
FWHM (arcsec)	$5''.5$	$5''.7$
Virtual pixel size (arcsec)	$9''.36 \times 9''.36$	$10''.4 \times 9''.56$
Detector	Si:As/CRC-744 (256 × 256)	
Conversion factor	$\sim 6e^-/ADU$	
Dark current	$< 30e^-/sec$	

FOVs and scales are formatted as cross-scan × in-scan.

---

[5] FIS scanned area is about 94% and IRC scanned area is expected to be almost the same.

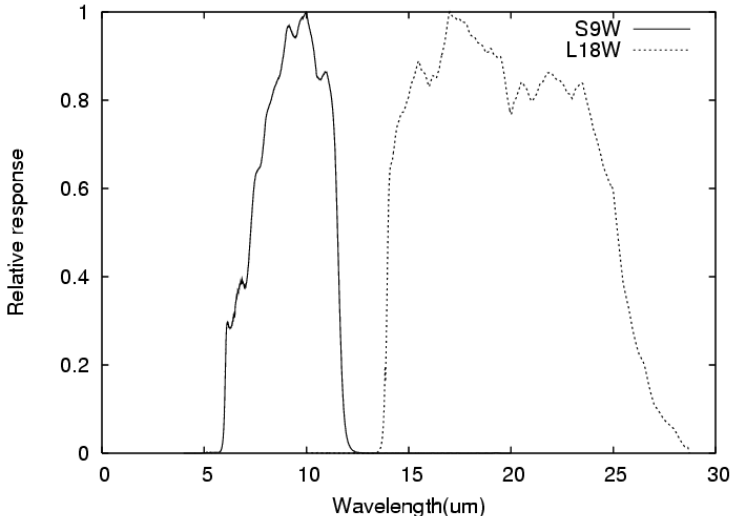

Figure 1: Relative Spectral Response Function of the IRC All-Sky Survey

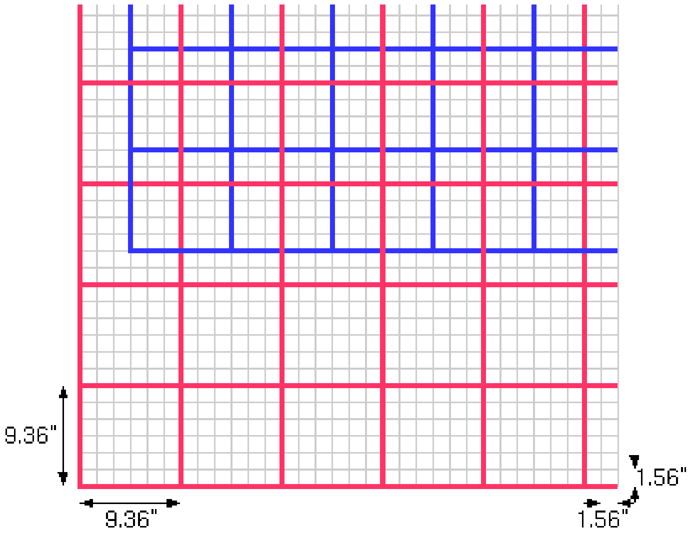

Figure 2: Virtual pixel alignment : Red lines show virtual pixels from the first sampling row, blue lines show virtual pixels from the second sampling row, and gray lines show the final output pixels after the data reduction processes.

A special read-out operating mode has been adopted for the All-Sky Survey observations (Ishihara et al. 2006). In this mode, pixels in 16 rows (Y=113 to 128) of total 256 rows are selected to output the signal and only the data from pixels in 2 rows (Y=117 and 125) are taken for the observation. Other pixels are not selected individually to shorten the sampling period. For each used pixel, the output signal is sampled 306 times non-destructively, and the pixel is reset. The row direction corresponds to the cross-scan direction. The scan speed is about 215 arcsec/sec and the sampling period of the output signal is 44 ms. Integration time at a point on sky is determined by the pixel field of view and scan speed, whereas spatial sampling in the scan direction is determined by the sampling rate and scan speed. The data of every four adjacent pixels are binned together (added and 2 bit-shifted to divide by four). In this process, output data consists of a virtual pixel, whose size is about 4 × 4 of the original pixel. Data from two rows enable the seconds confirmation (though the time difference is about 87ms). In addition, sampling timing and binning group of pixels are chosen such that the virtual pixels cover a staggered grid of the sky (Figure 2). Image strips of 64 × 306 virtual pixels from the first sampling row and those of 63 × 306 virtual pixels from the second sampling row for each band are the basic unit of the data.

2 Outline of data processing

Figure 3 shows the flow of the data processing. First, we extract the IRC All Sky Survey data from the packets and reformat into FITS image format data. Each FITS file contains on chip integrating data within an interval of resets for each band. From this data, image strips are generated after removal of instrumental anomaly effects. Each image strip has a field of view of 10' × 40' corresponding to the scan area. There are two frames corresponding to two detector rows used by scan observations for each band. Point-like sources are extracted using the source extractor (SExtractor: Bertin & Arnouts 1996). A region with connected pixels above 3 sigma threshold is a candidate. The two frames are combined into one frame with one sixth virtual pixel size. From the combined frame, point-like sources are extracted again using SExtractor. At this time, a region connected at least 32 pixels above 3 sigma threshold is a candidate. Then we have point source candidates from row #1 data (candidate1), candidates from row #2 data (candidate2), and candidates from combined frame (candidate3). Candidate3 are the basic entries of our source list and each candidate is confirmed examining entries in candidate1 and candidate2. This confirmation is the so called 'second confirmation' where the time shift is only 87 ms. The valid observed area is marked with the same pixel size as the combined image. This called a Norb map, which means number of observations. Point-like sources are listed in the event list and used as one of the input data for the pointing reconstruction process. After the pointing reconstruction process, all events have reconstructed position data. Then, fluxes of the point source events are calibrated. In parallel, WCS (world coordinate system) of Norb maps are adjusted by the result of the pointing reconstruction. From the calibrated point source event list and Norb maps, point source catalogue is generated.

In this version we have the following problems in the basic process described above. 1) In the second confirmation process, we cannot rule out some fake detections because of a coding error. Some fake sources may be mixed into the point source event list. 2) Reset anomaly and linearity corrections limit the accuracy. Errors in these corrections limit the repeatability of the detected source flux. 3) Norb maps are not generated for the whole sky. In this version, the number of observations for a given sky position is not available. Therefore, NSCANP09 and NSCANP18 (see Table 4) in this version of the catalogue are not available.

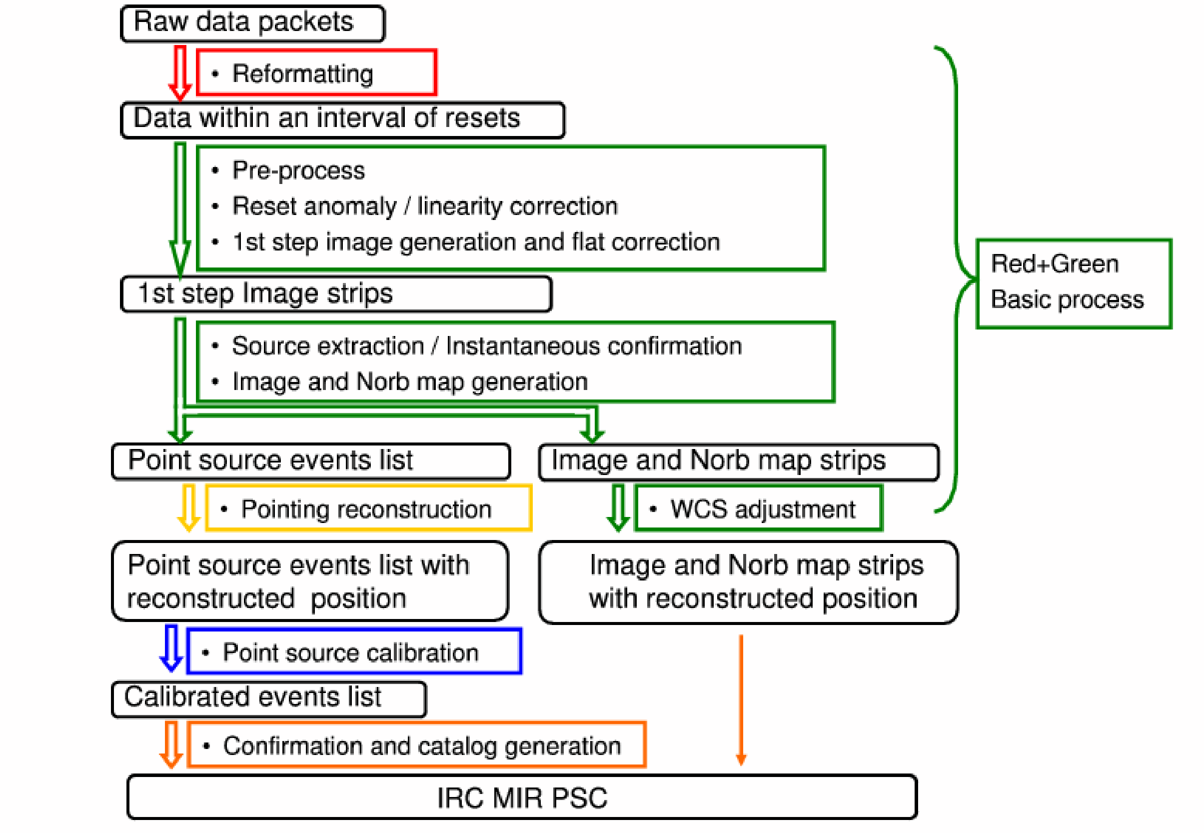

Figure 3: Data processing flow

3 Pointing reconstruction

The pointing reconstruction, that is the determination of the scan position during the survey, is carried out as follows. Information of satellite attitude determined by the onboard computer is stored in the AOCS telemetry, together with the data from the AOCS sensors. The Groundbase Attitude Determination System (G-ADS) works with these data. Onboard ADS and G-ADS data are similar to each other, as they are based on the same sensor data, however, G-ADS processing is more carefully done and should be more reliable.

The remaining major source of uncertainty is the alignment between the AOCS system and the telescope axis, and its time variation. This is solved by the pointing reconstruction processing. The AKARI team in the ESA's European Space Astronomy Centre (ESAC) is in charge of this processing. Input data are G-ADS attitude, ephemeris data, Focal-plane Star Sensor (FSTS) scan data, the IRC All-Sky Survey point source event list, and input reference catalogues. The output returned from the processing are survey attitude information and identification list of the IRC event. The latter contains positions of all events in the input list, and is used for generating the AKARI/IRC PSC.

Two input reference catalogues are generated for AKARI pointing reconstruction: (i) the near-infrared FSTS Reference Catalogue, and (ii) the mid-infrared IRC Reference Catalogue. FSTS Reference Catalogue has a total of 2,862,152 sources brighter than the 10th magnitude in the J-band in the 2MASS Point Source Catalogue. 1,327,581 sources were cross-matched against the Tycho-2 astrometric catalogue to improve the astrometric information. The IRC Reference Catalogue is composed by: (i) the whole MSX Infrared Astrometric Catalogue; (ii) the whole MSX Point Source Catalogue; and (iii) sources detected by IRAS for which a clear counter part exists in the 2MASS Point Source Catalogue at high galactic latitudes. The total number of entries is 670,833.

The Pointing Reconstruction software *PRESA* provides the transformation between the G-ADS and the Focal Plane attitude. The combination of a forward and a backward continuous-discrete Kalman filter is used to estimate the transformation quaternion from G-ADS to the Focal Plane attitude.

Figure 4 demonstrates the pointing reconstruction performance. The plot shows the fraction of the IRC events with error smaller than the given values. The error is the distance between the positions determined from the pointing reconstruction results and those from the position reference catalogue. For fair evaluation, the pointing reconstruction for this test was carried out using randomly selected sources amounting to half of the catalogue, then the positions of the sources from the other half catalogue are determined for the evaluation. The error includes pointing reconstruction processing error and the measurement error. For the brightest sources the measurement error should have minor contribution, and we can conclude that the position accuracy is better than three arcsec in 95 per cent of the events (c.f., original requirement was 3 and 5 arcsec in the in- and cross-scan direction in the final version).

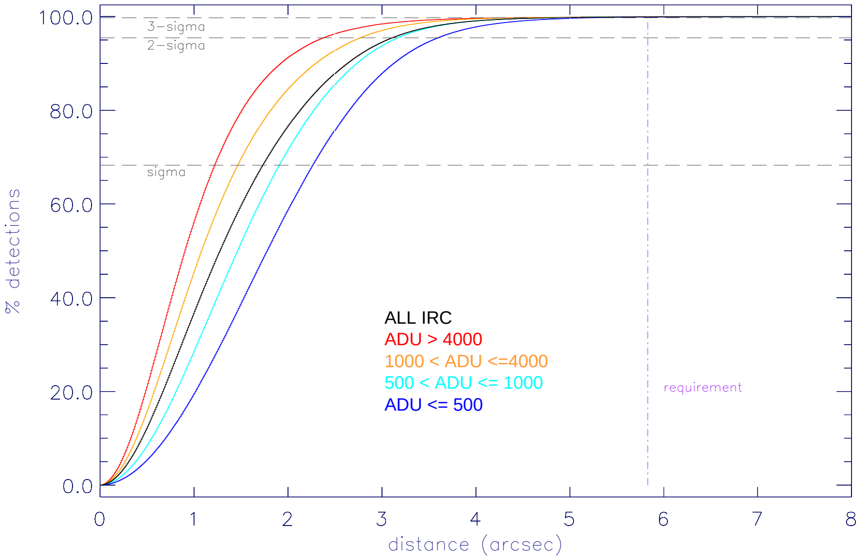

Figure 4: Statistical error of the pointing reconstruction using 50% of the catalogue data. The error for events in remaining 50% data is defined as the distance between the position determined by pointing reconstruction and the position of the input reference catalogue. The lines show the fraction of the IRC events with an error smaller than given values. Color of lines denotes the flux range of events.

4 Flux calibration

Standard stars for the absolute flux calibration were selected from standard stars in Cohen et al. (1999), those in the ecliptic pole regions (Cohen et al. 1996, 1999, 2003a, 2003b; Cohen 2003), those in the LMC (Meixner et al. 2006; Cohen et al. 2003b), and those for the calibration of ISO (Cohen et al. 1995). The flux ranges of the stars in Cohen et al. (1999) are 5 – 200 Jy and 1 – 40 Jy in the S9W and L18W bands, respectively. Standard stars in the North and South Ecliptic Pole (NEP and SEP) regions and LMC/SMC regions that are established by M. Cohen for the calibration of the Spitzer/IRAC are also used for faint-end calibration. The flux ranges of these stars are 0.01 – 1 Jy and 0.003 – 0.3 Jy in the S9W and L18W bands, respectively. Several bright standard stars established by M. Cohen for the calibration of ISO instruments are also used for bright-end calibration. The flux ranges of these stars are 75 – 520 Jy and 17 – 280 Jy in the S9W and L18W bands, respectively. We identify the events whose position offsets are less than 5 arcsec for the input standard stars and obtain their output ADUs. We disregard data that are obviously mis-identified judging from fluxes.

The in-band flux density of each band at the effective wavelength, $f_\lambda^{quoted}(\lambda)$ is calculated by the following equation:

$$f_\lambda^{quoted}(\lambda_i) \quad = \quad \frac{\int_{\lambda_{is}}^{\lambda_{ie}} R_i(\lambda)\lambda f_\lambda(\lambda) d\lambda}{\int_{\lambda_{is}}^{\lambda_{ie}} (\frac{\lambda_i}{\lambda}) R_i(\lambda)\lambda d\lambda} \tag{1}$$

where $f_\lambda(\lambda)$ is the flux density of a standard star SED (Cohen template) and $R_i(\lambda)$ is the spectral response function (the transmission of the optics and the response of the detector, unit: electron·photon^{-1}) of the band i. Here $f_\lambda \propto \lambda^{-1}$ is assumed. This is the convention adopted by IRAS, COBE, ISO, Spitzer/IRAC, and AKARI IRC pointing observation (Tanabé et al. 2008). The adopted effective wavelengths of each band, λ_i are listed in Table 2 along with the range of the integration (λ_{is}, λ_{ie}).

Table 2: The effective wavelengths λ_i and the range of the integration,λ_{is}, and λ_{ie}

band	λ_i	λ_{is}	λ_{ie}
S9W	9.00	2.50	23.510
L18W	18.00	2.58	28.720

The relations between pipeline output ADUs of events and calculated in-band fluxes of the standard stars are shown in Figures 5 and 6 for the S9W and L18W bands. The relations are nearly linear but we can see systematic difference from the linear relation (bottom right panels in the figures) which suggest that the flux conversion should be made with non-linear functions.

We assume a conversion function as a linear function in log-log scale;

$$\ln(\mathrm{Flux}) \quad = \quad \sum_i a_i (\ln(\mathrm{ADU}))^i \tag{2}$$

i.e

$$\mathrm{Flux} \quad = \quad \exp\left(\sum_{i=0}^{2} a_i (\ln(\mathrm{ADU}))^i\right) \tag{3}$$

where Flux denotes flux in Jy unit and ADU denotes output digital counts from the pipeline. The coefficients of the function were derived from least square fitting between pipeline output ADUs and calculated in-band fluxes of the standard stars. Derived coefficients for S9W and L18W are shown in Table 3.

Table 3: Coefficients of the conversion function for S9W and L18W

band	a_2	a_1	a_0
S9W	0.00850918	0.806013	-7.66656
L18W	0.00717589	0.829091	-7.35238

The best-fit functions are shown in Figures 5 and 6. The deviations of the fluxes converted with the derived conversion functions are shown in the bottom panel of the figures. The deviations seems flat and the fluxes converted with the derived functions reproduce satisfactorily the in-band fluxes. We adopt these functions as conversion functions for the point sources. But we should note that the conversion functions are applicable for the point sources whose fluxes are up to 500 Jy in the S9W band and up to 300 Jy in the L18W band because of the limits in the calibration standard.

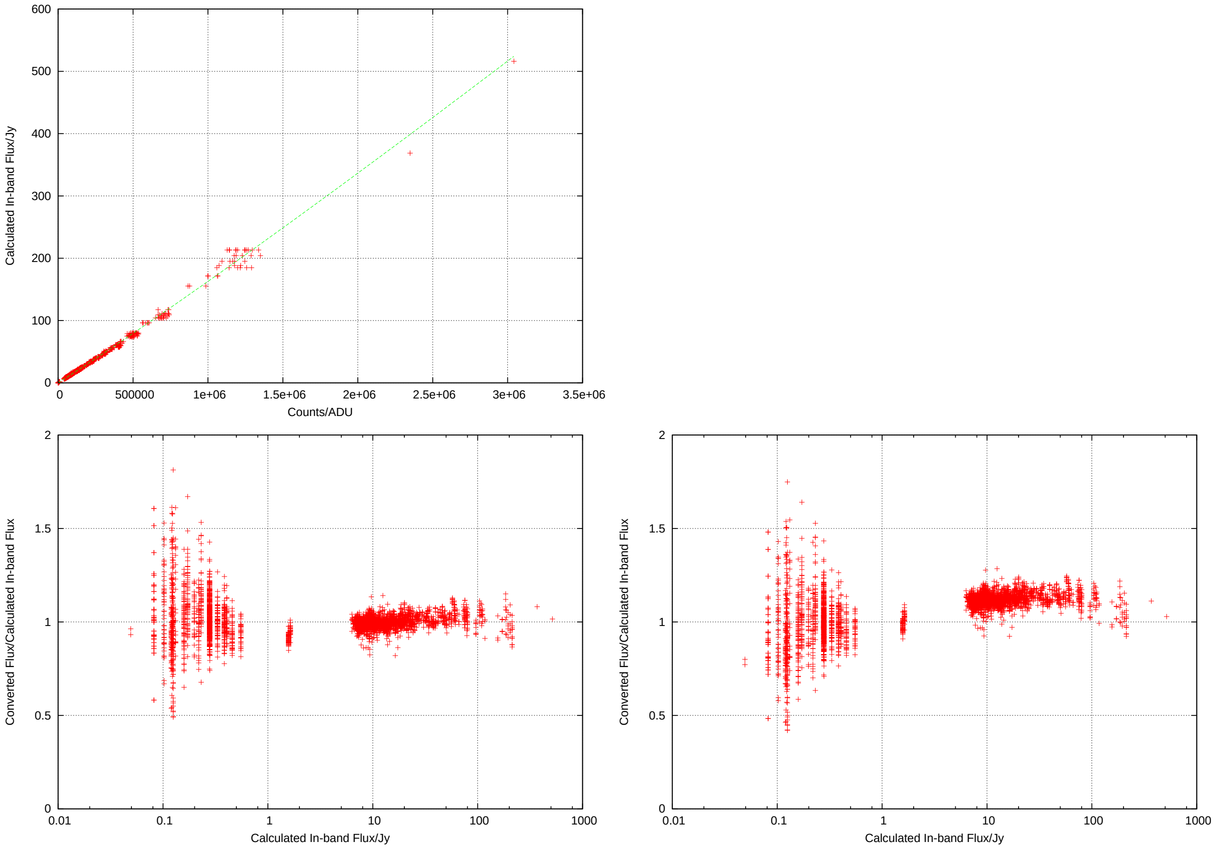

Figure 5: Top: The pipeline output ADUs of events is plotted as a function of the calculated in-band fluxes of the standard stars in the S9W band. Derived non-linear conversion function for S9W band are over plotted. Bottom left: The deviations of the ratio of calibrated fluxes with the non-linear conversion function over model fluxes of the standard stars. Bottom right: The deviations of the same as left but linear conversion function is assumed.

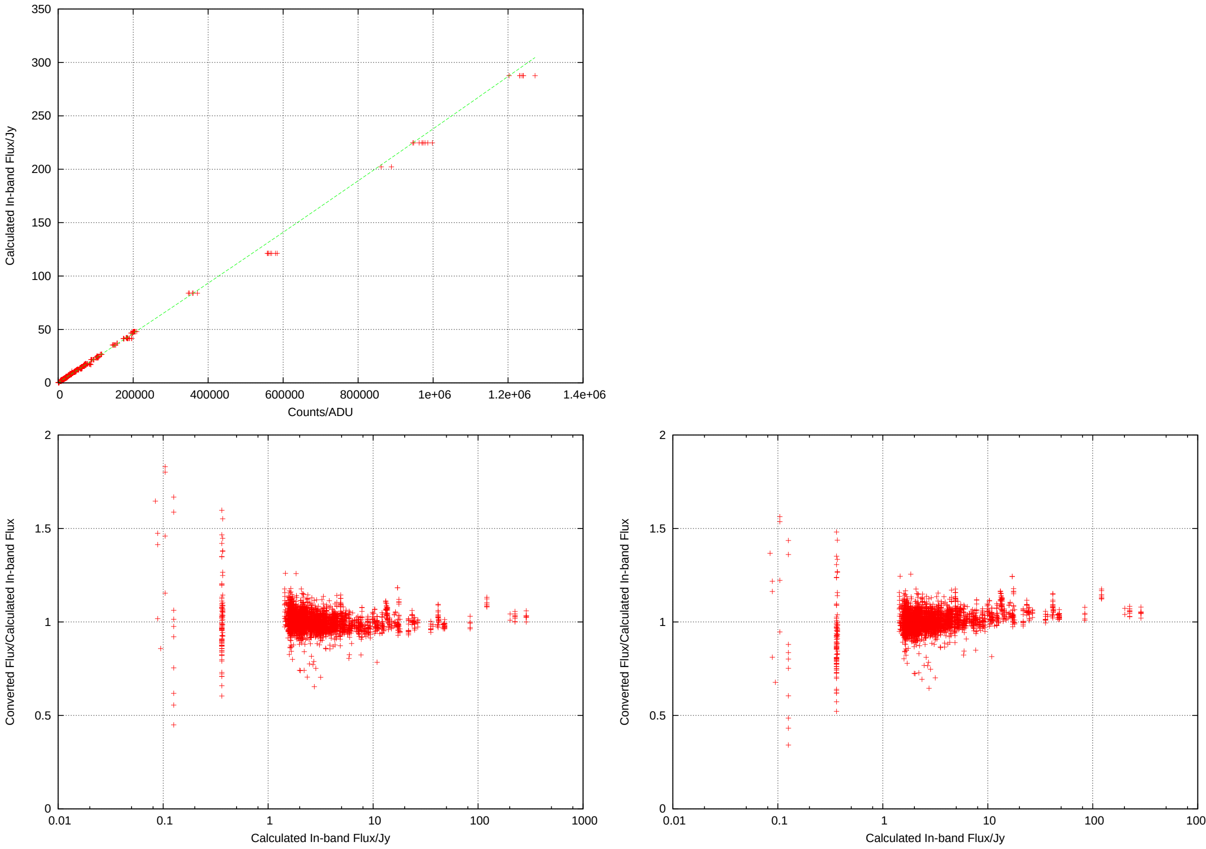

Figure 6: Top: The pipeline output ADUs of events is plotted as a function of the calculated in-band fluxes of the standard stars in the L18W band. Derived non-linear conversion function for L18W band are over plotted. Bottom: The deviations of the ratio of calibrated fluxes with the non-linear conversion function over model fluxes of the standard stars. Bottom right: The deviations of the same as left but linear conversion function is assumed.

5 Catalogue generation

In the position calibrated events list, a group of events whose positions are within a threshold value is recognized as a source. In this "grouping" process, radius of 5 arcsec is employed as a threshold value. Events affected by the South Atlantic Anomaly (SAA) have been excluded in this process. Grouping was done in the S9W band and in the L18W band independently. After the first grouping process, distance from a source candidate to the nearest one is checked and if there are more than two groups within 7 arcsec, we consider them as a single source with some outskirt events. In this case we take the group with maximum number of events as a source candidate and discard other groups. Then, the source list in the S9W band and that in the L18W band are merged into one list. Sources within 7 arcsec are treated as the same source in both band. Position (RA, DEC) and position error (POSERRMJ, POSERRMI, POSERRPA: see section 6) are calculated from events in the S9W band only, if the number of available data is larger than or equal to 2. Otherwise, these data are calculated from events in the L18W band only. We do not merge position data from two bands. Flux in the catalogue is calculated as a mean value of FLUX_AUTO, measured by SExtractor (see SExtractor v2.5 user's manual). Event data near the edge of the image strips are excluded from flux calculation with exceptional case that there is only one or zero events available. This exceptional case is notified by FLAG09 and FLAG18 entry of the catalogue. The mean values of fluxes and associated errors (standard deviations of the mean) are defined as:

$$< X > \;=\; \mathrm{MEAN} = \frac{\sum_i^N X_i}{N} \tag{4}$$

$$< \sigma > \;=\; \mathrm{ERROR} = \sqrt{\frac{\sum_i^N (X_i - < X >)^2}{N(N-1)}} = \frac{\mathrm{r.m.s.}}{\sqrt{N}} \tag{5}$$

where N is the number of data.

6 Catalogue contents and format

The contents of the current version AKARI/IRC PSC are summarized in Table 4. The catalogue will be distributed in two ways: a FITS file and access via DARTS database query. DARTS interface will be provided later. The current version does not include complete information. The contents and format are carefully defined for permanent use, but we do not rule out the possibility of future updates according to the user's feedback or technical progresses.

Table 4: Contents of the AKARI/IRC Point Source Catalogue

Name	Type	Format code	Unit	Description
OBJECTID	short	I		AKARI source ID number.
NAME	string	14A		AKARI source name. The format is HHMMSSS+/-DDMMSS
RA	double	D	degree	Right Ascension (J2000)
DEC	double	D	degree	Declination (J2000)
NDATA_POS	short	I		Number of events which are used for positional calcuration
POSERRMJ	float	E	arcsec	Major axis of position error ellipse
POSERRMI	float	E	arcsec	Minor axis of position error ellipse
POSERRPA	float	E	degree	Position angle of Major axis
FLUX09	double	D	Jy	Flux density in S9W
FLUX18	double	D	Jy	Flux density in L18W
FERR09	double	D	Jy	Flux error in S9W
FERR18	double	D	Jy	Flux error in L18W
FQUAL09	short	B		Flux quality flag for S9W (These entry is reserved in future.)
FQUAL18	short	B		Flux quality flag for L18W (These entry is reserved in future.)
FLAGS09	short	B		Bit flags data quality for S9W. 1: not month confirmed, 2: saturated (not used in this version), 4: use SAA (not used in this version), 8: use edge
FLAGS18	short	B		Bit flags data quality for L18W. 1: not month confirmed, 2: saturated (not used in this version), 4: use SAA (not used in this version), 8: use edge
NSCANC09	short	I		Number of scans in which the source is detected for S9W
NSCANC18	short	I		Number of scans in which the source is detected for L18W
NSCANP09	short	I		Total number of scans that possibly observed the source for S9W (not used in this version)
NSCANP18	short	I		Total number of scans that possibly observed the source for L18W (not used in this version)
NDATA09	short	I		Total number of events that contribute to the measurements for FLUX09
NDATA18	short	I		Total number of events that contribute to the measurements for FLUX18
MCONF09	short	I		1 is month confirmed and 0 is not. Inverted value of 1st bit of FLAG09
MCONF18	short	I		1 is month confirmed and 0 is not. Inverted value of 1st bit of FLAG18
FDENS09	short	I		Number of sources in 30 arcsec radius for S9W
FDENS18	short	I		Number of sources in 30 arcsec radius for L18W
EXTENDED09	short	B		Extended source flag
EXTENDED18	short	B		Extended source flag
MEAN_AB09	float	E	arcsec	The average of major and minor axes of source extent for S9W
MEAN_AB18	float	E	arcsec	The average of major and minor axes of source extent for L18W
FVAR09	short	B		Variability flag (not used in this version)
FVAR18	short	B		Variability flag (not used in this version)

Description

OBJECTID
Source ID number.

NAME
Source name from its J2000 coordinates, following the IAU Recommendations for Nomenclature (2006). The format is HHMMSSS±DDMMSS, e.g., 0123456+765432 for a source at (01h23m45.6s, +76d54m32s). The source must be referred to in the literatures by its full name: AKARI-IRC-b1 J0123456+765432, where b1 refers to the version code.

RA, DEC
J2000 Right Ascension and Declination of the source position in degree.

NDATA_POS
Number of events used to calculate the mean coordinates. If the source has more than two available S9W events, the position is estimated from S9W events only, else the position is estimated from L18W events, i.e.
NDATA_POS = NSCANC09 for NSCANC09 ≥ 2
NDATA_POS = NSCANC18 for NSCANC09 < 2

POSERRMJ, POSERRMI, POSERRPA
One-sigma error of the source position expressed by an ellipse with Major and Minor axes [arcsec], and Position Angle [deg; East from North].

FLUX09, FLUX18
Flux density of the source in the two IRC bands in Jansky.

FERR09, FEROR18
Flux error in the two IRC bands. Errors are defined as equation 5.

FQUAL09, FQUAL18
Flux density quality flag in the two IRC bands. No data in the current version catalogue.

FLAGS09, FLAGS18
Bit flags of data quality:
1(LSB): not month confirmed
This means that the period between the first detection and the last detection is shorter than a month.
2: saturated (not used in this version)
4: use SAA (not used in this version)
8(MSB): use edge events
If the number of events is too small, we use the event data near the edge of the image strip. In this case, this flag warn you of underestimation of the flux.

NSCANC09, NSCANC18
Number of scans on which the source is detected. NSCANC is less or equal to NSCANP.

NSCANP09, NSCANP18
The number of times the source position has been scanned during the survey.

NDATA09, NDATA18
Number of events that contribute to the flux measurements in the two bands. Normally, events

near the edge of the image strip are excluded from the measurements. Note that if only 0 or 1 event are available, the flux is computed also from edge events.

FDENS09, FDENS18
The number of sources in 30 arcsec radius.

MCONF09, MCONF18
1 is month confirmed and 0 is not. Inverted value of LSB of FLAGSxx.

EXTENDED09, EXTENDED18
The flag indicates that the source is possibly more extended than the point spread function. This is "TRUE" when MEAN_AB > 15.6

MEAN_AB09, MEAN_AB18
The average of radius along major and minor axes of images, i.e. $(< a > + < b >)/2$ where $< a >$ and $< b >$ are the mean semi-major and semi-minor axis lengths of images estimated by SExtractor.

FVAR09, FVAR18
Variability flag. Not available in this version.

7 Performance

7.1 Number of sources

The AKARI/IRC Point Source Catalogue contains 877091 sources, out of which 851189 are detected in the S9W band and 195893 in the L18W band. Observations exist in both bands for 169990 sources. As shown in Table 5, by far the largest fraction of sources is detected in the flux range 0.1 to 1 Jy (73% at S9W and 76 % at S18W).

Events affected by the South Atlantic Anomaly (SAA) are excluded from the catalogue.

Table 5: Number(N) of detected sources as a function of flux level

Range Jy	N (S9W)	N (L18W)
0 − 0.1	150047	1373
0.1 − 1	622577	149842
1 − 10	71510	39419
10 − 100	6603	4768
100 − 1000	449	481
> 1000	3	10
total	851189	195893

Table 6: Number of cross matches of the AKARI/IRC PSC with 2MASS, MSX, and IRAS sources.

Survey	Number of Sources	Search radius	Matching Sources
2MASS	2862152	$3''$	720942
MSX	323052	$3''$	104934
IRAS PSC	245889	$20''$	134533

Table 6 provides the results of a cross correlation between the AKARI/IRC PSC and the 2MASS, MAX and IRAS surveys. For the 2MASS catalogue, the search has been limited to magnitude J = 10.

7.2 Extended sources

Figure 7 shows the dependence of MEAN_AB on flux. This figure provides the possibility of distinguishing between two populations of sources: extended and point sources. In this version of the catalogue, extended sources are defined as those with MEAN_AB $\geq$ 15.6 [arcsec], and the associated EXTENDED flag is set to unity. This flag is based on a fixed threshold value. We note, however, that also bright point source might appear as extended. The histogram in Figure 8 shows clearly that the distribution of these parameters is dominated by point sources.

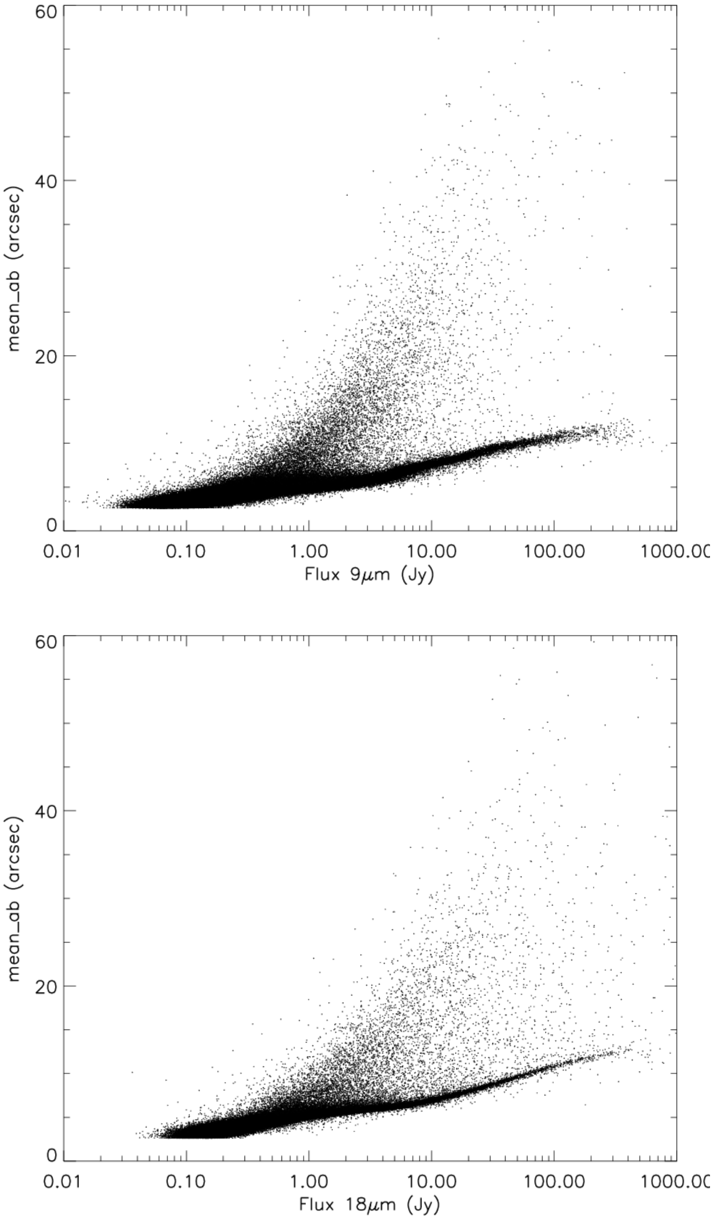

Figure 7: MEAN_AB as a function of the S9W (top) and L18W (bottom) flux.

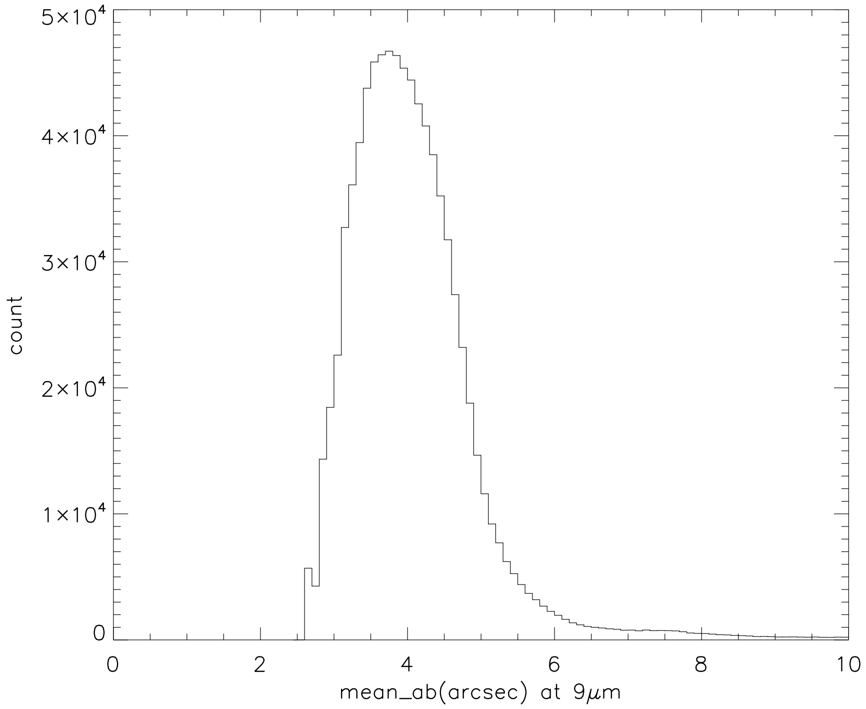

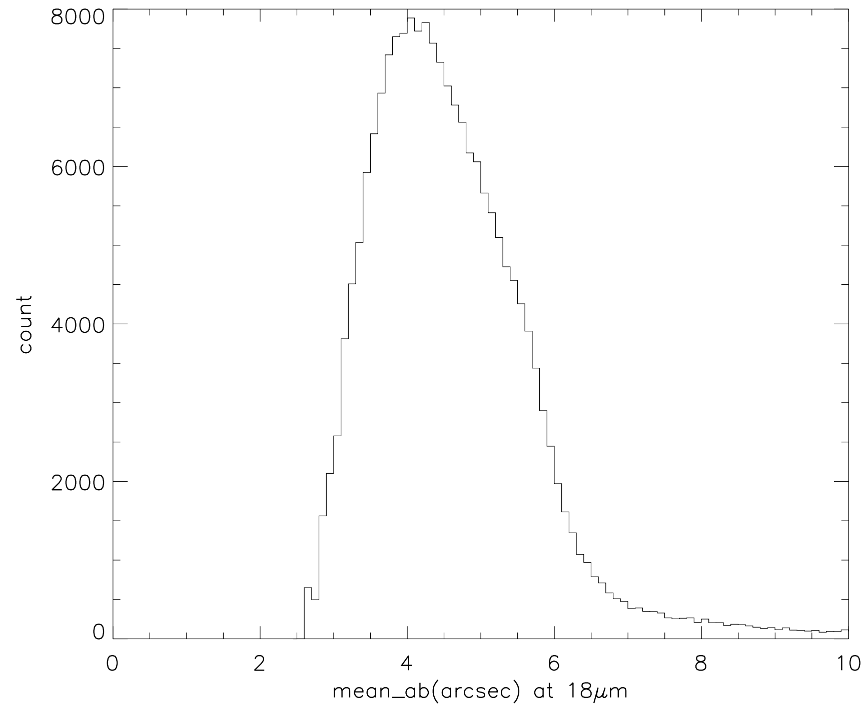

Figure 8: Histogram of MEAN_AB for S9W (top) and L18W (bottom).

7.3 Accuracy of coordinates

For a given source, the distribution of the repeatability errors on coordinates can be described as an error ellipse, whose minor and major axis are defined as the observed minimum and maximum standard deviation of the distribution, and the position angle is that of the major axis. A test of the internal accuracy of AKARI coordinates is given Figure 9, showing the minor axis of the error ellipse as a function of that of the major axis. One can easily appreciate that the errors cluster around $0.2''$–$0.3''$.

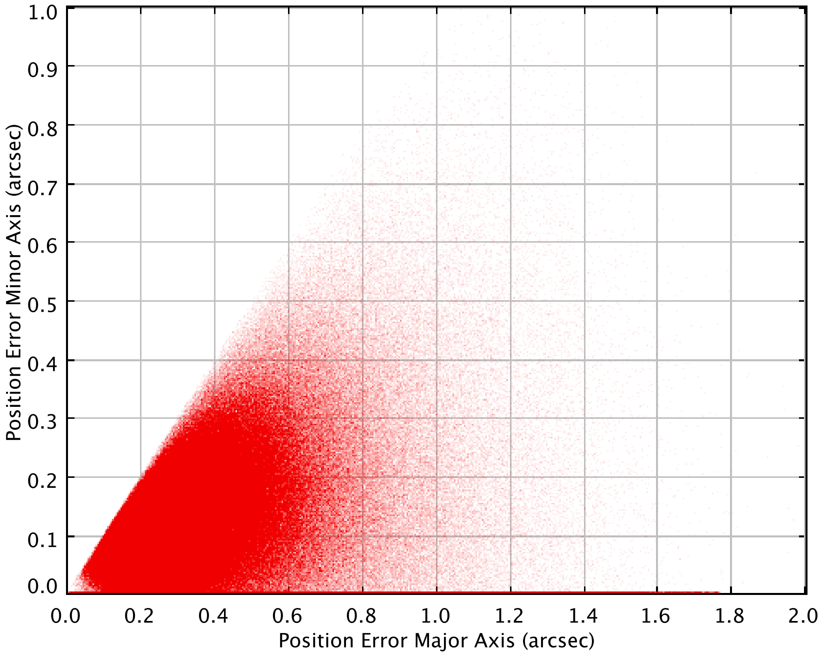

Figure 9: Position repeatability. Radius size of error ellipsoid estimated from the positions of events attributed the same object is plotted as a point

We have tested the accuracy of coordinates of the AKARI/IRC PSC sources through a cross-match with the the 2MASS survey. Figure 10 show the number AKARI/IRC PSC sources matching with the 2MASS J, H and K survey as a function of the seach radius. While too many sources remain unmatched for the case of search radius is $1''$, there is no substantial gain by increasing it above $3''$, a value that is adopted in the following.

Figure 11 shows the histogram of the angular separation between the AKARI/IRC PSC coordinates and the 2MASS reference coordinates for cross matched sources. According to these data, nearly 95% of the sources have an angular separation $\leq 2''$, while about 73 % have a separation $\leq 1''$. The mean angular separation between AKARI and 2MASS coordinates of the same sources is 0.765 $\pm$ 0.574 arcsec. Larger internal errors are of course expected for fainter sources, as shown in Figure 12.

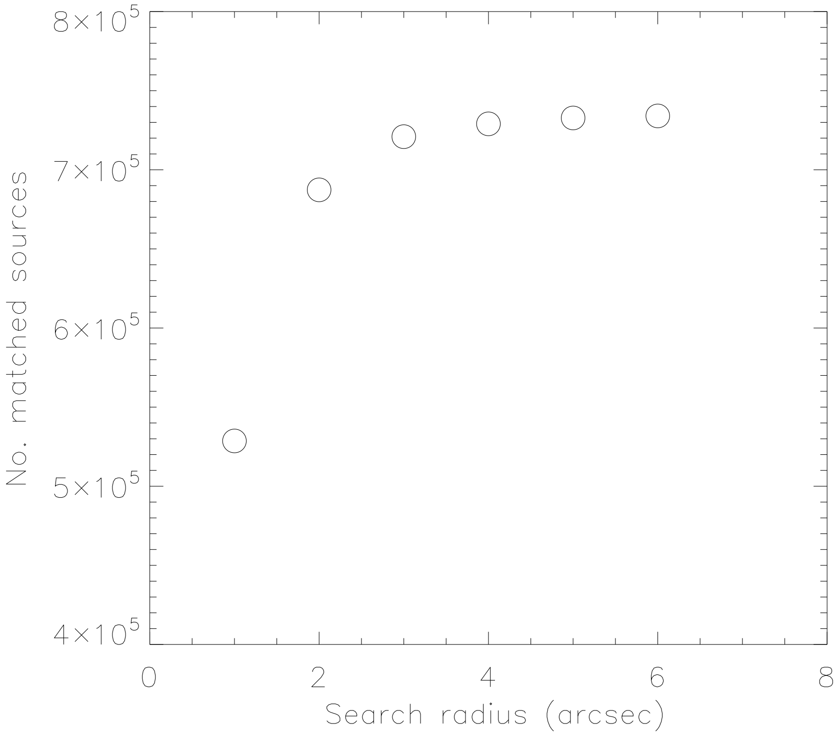

Figure 10: Number of AKARI/IRC PSC sources matching the 2MASS catalogue as a function of search radius.

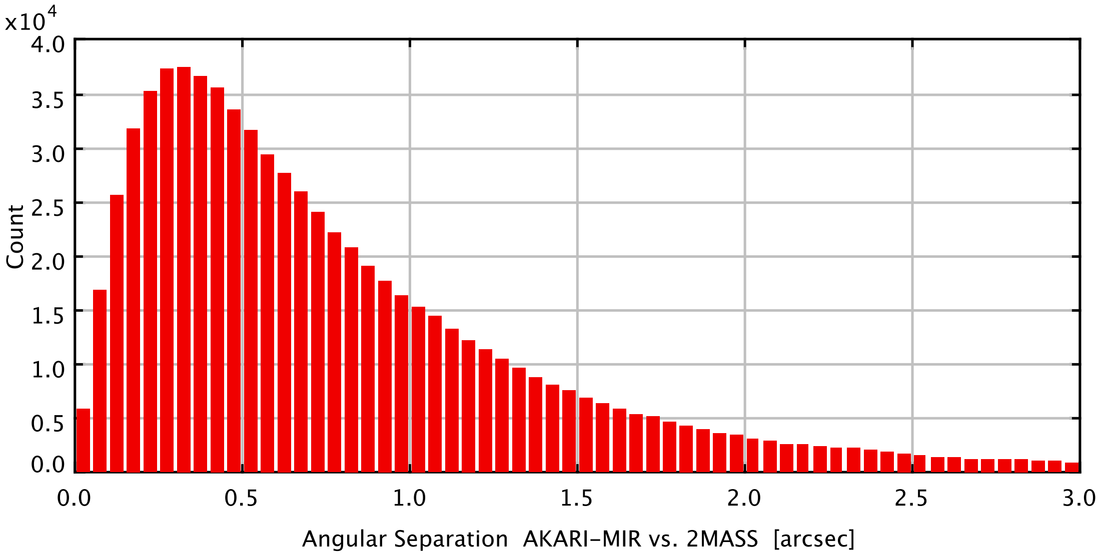

Figure 11: Histogram of the angular separation between AKARI PSC coordinates and the 2MASS coordinates for the common sources.

7.4 Flux Accuracy

There are basically two ways to assess the flux accuracy. The first consists of a repeatability test in which the internal accuracy of fluxes is measured through the rms errors on mean fluxes for sources observed more than once. The second, after applying the flux calibration, consists in comparing flux-calibrated photometry with the known fluxes of standard stars.

Figure 13 shows the relative errors (FERR09/FLUX09 and FERR18/FLUX18) as a function of flux for all sources with positive flux. As expected, larger errors are seen at lower flux levels. However, the probability of observing large errors is rather small, as shown in the histograms in Figure 14. The figure shows indeed that for the most probable error is around 2 – 3 %. For about 80 % of the data the relative errors are smaller than 15%, and for about 96% are smaller than 30%. At this stage, we cannot quantify how variable objects artificially contribute to increase the scatter on observed fluxes.

The data in Figure 14 can be used also to compute the typical Signal-to-Noise ratio (S/N) to be associated with different flux levels. This is done in Figure 15, which shows S/N as a function of the flux. The figure indicates that for the faintest sources with $\sim$ 0.045 Jy in the S9W band, the expected S/N is $\sim$ 6, while it is $\sim$ 3 for $\sim$ 0.06 Jy in the L18W band. The figure shows as well that S/N increases with increasing flux and then from flux above 0.6Jy / 0.9Jy S/N become constant or slightly decrease at $\sim$ 20 / $\sim$ 15 for S9W / L18W respectively. These S/N limitation comes from the accuracy limits in the data reduction process. Errors in the correction of detector reset anomaly, linearity, and individual sensitivity of pixel cause the fluctuation of the detection flux and limits the repeatability of the flux measurements.

The flux calibration and linearity correction applied on event list data are described in section 4. Here, Figure 16 provides a test of the accuracy of the flux-calibrated data after the catalogue generation in the two MIR bands. The full dynamical range of the MIR detectors cannot be fully explored with the standard stars that have been used, especially with respect to linearity properties.

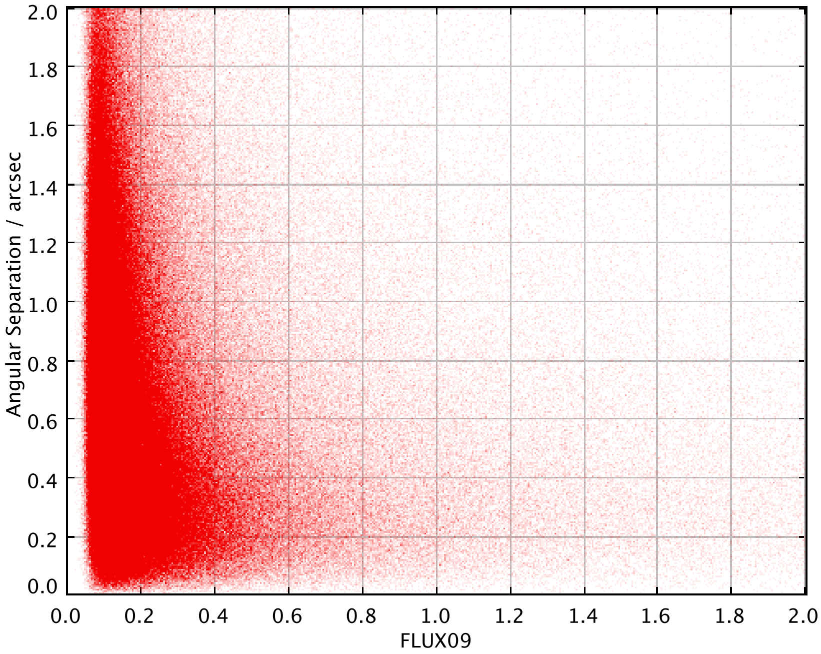

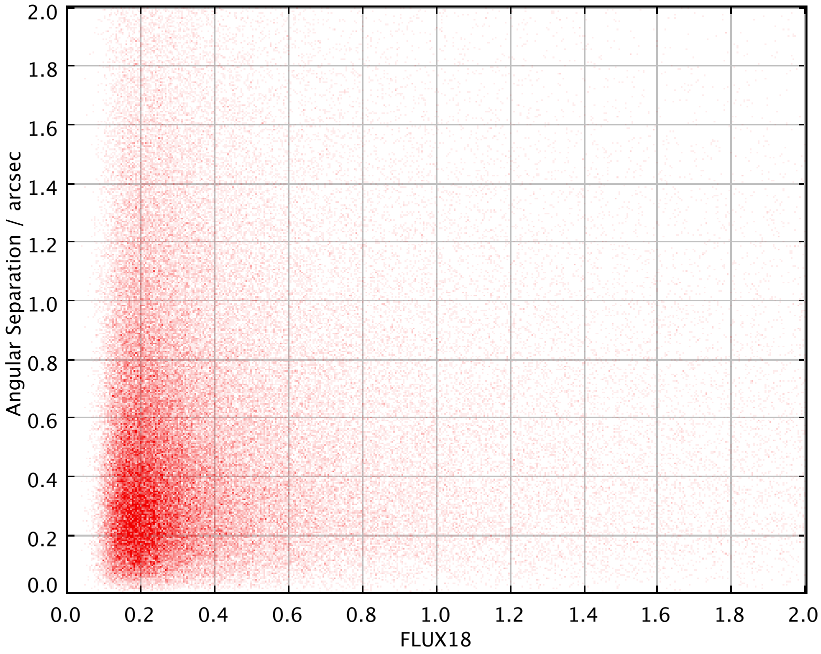

Figure 12: Angular separation between AKARI PSC coordinates and the 2MASS coordinates as a function of flux.

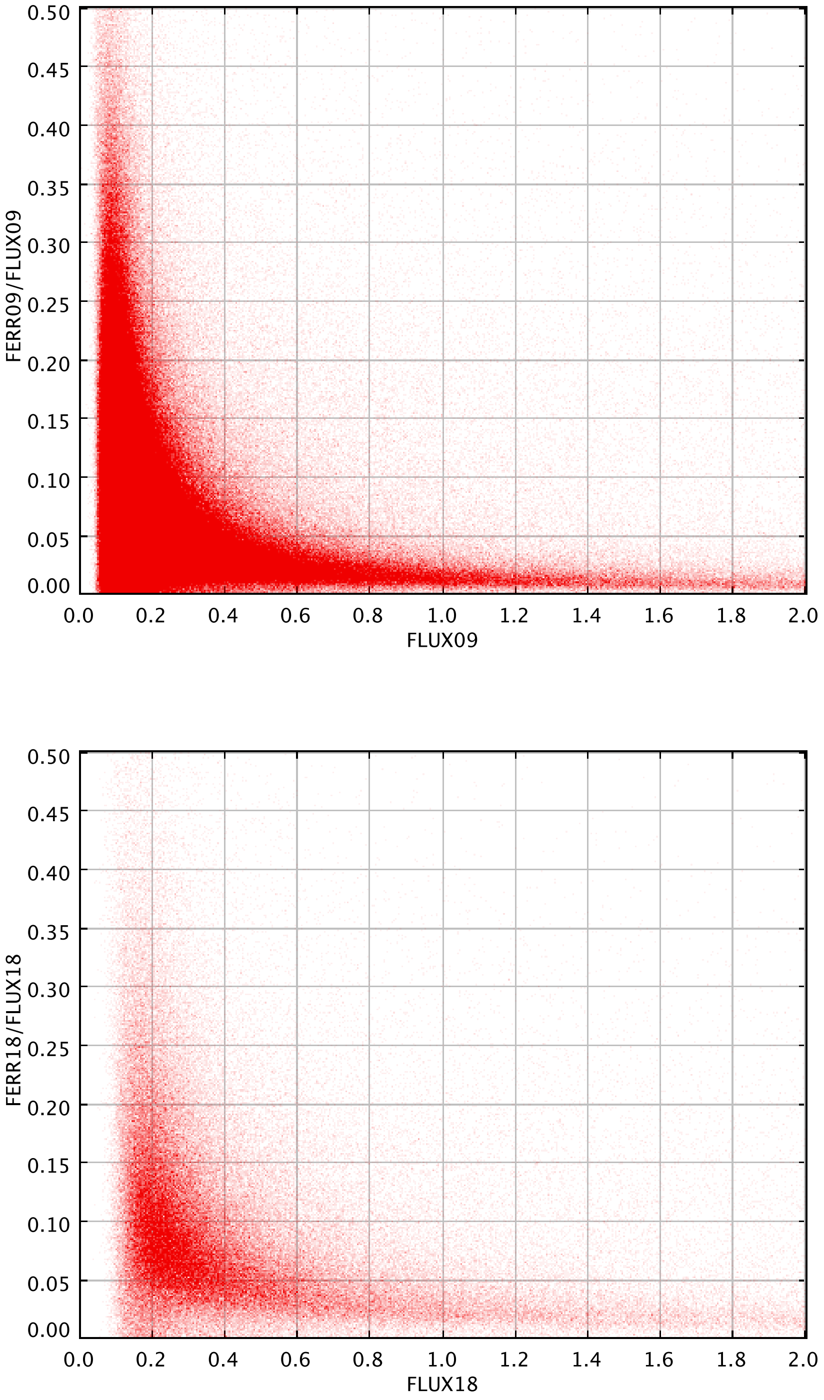

Figure 13: Internal relative errors on the S9W and L18W fluxes as a function of flux.

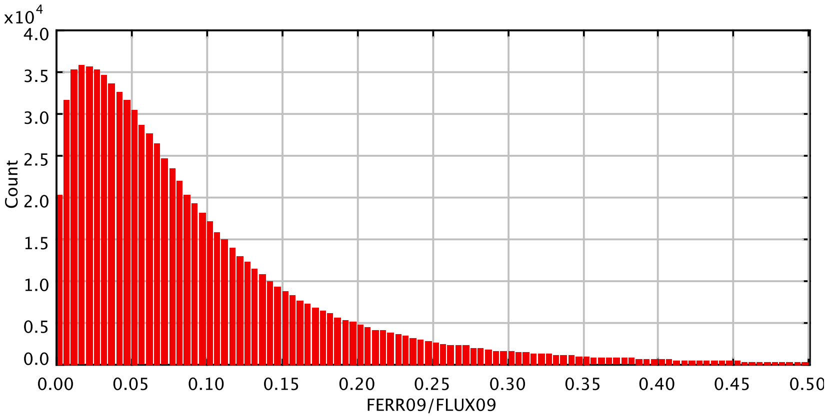

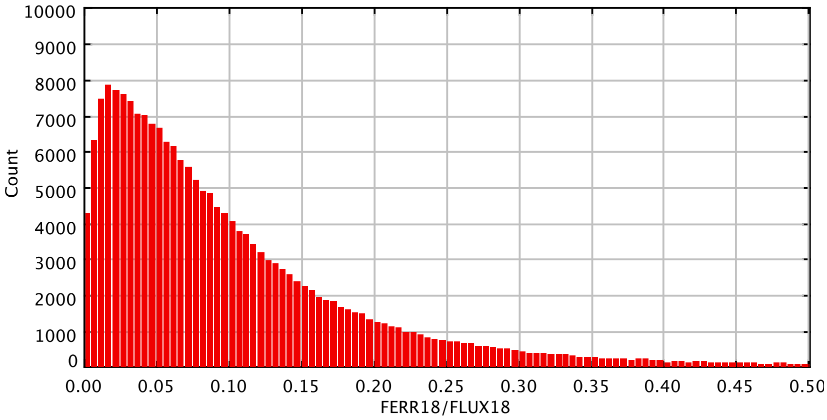

Figure 14: Histograms showing the distribution of internal relative error on the S9W and L18W band fluxes as a function of flux.

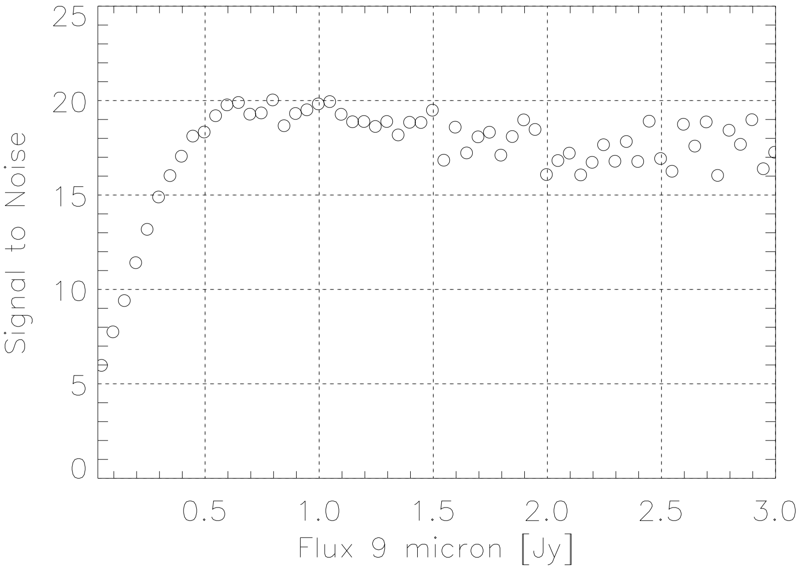

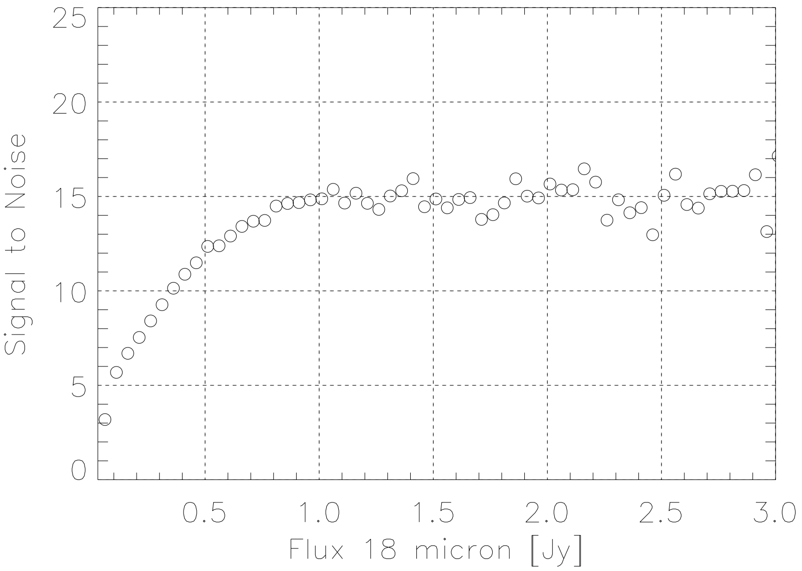

Figure 15: Signal to Noise ratio as a function of the S9W and L18W flux.

In any case, the overall performance in terms of linearity and self-consistency is good: in the flux range explored we find: $F_\nu^{AKARI}/F_\nu^{Standard} = 0.970 \pm 0.070$(rms) at S9W from 412 measurements, and $F_\nu^{AKARI}/F_\nu^{Standard} = 1.001 \pm 0.045$(rms) at L18W from 406 measurements.

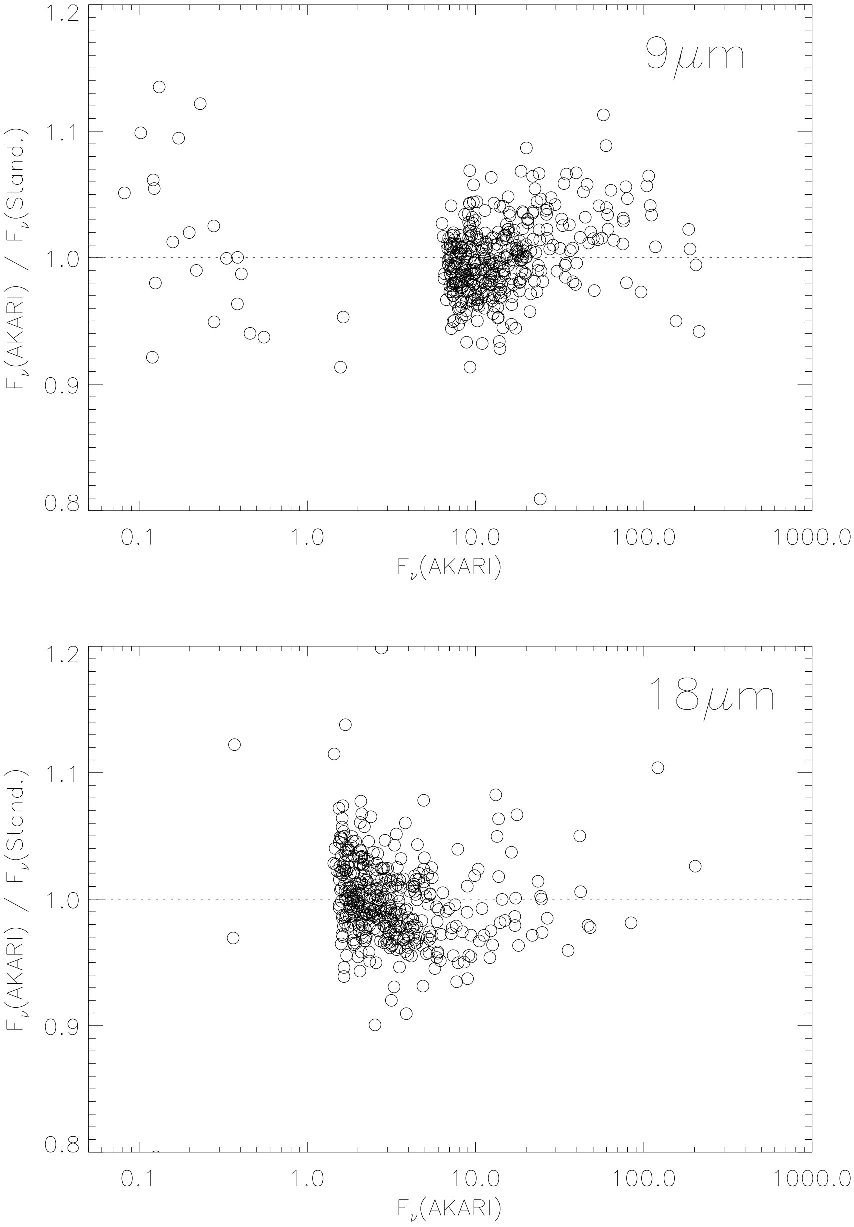

Figure 16: Flux ratio of AKARI/MODEL in the S9W and L18W bands. MODEL flux is calculated in-band flux of standard stars and AKARI flux is FLUX09 or FLUX18 in the catalogue. Note that FLUX09 and FLUX18 is the mean value of events fluxes, whereas Figure 5 and 6 use the fluxes of events.

7.5 Completeness

The completeness of a survey above a given flux level, is usually defined as the fraction of true sources that can be detected above that level. It is difficult to apply this concept to the AKARI survey because one should dispose of a statistically significant sample of true sources with known IRC fluxes. The standard stars used for the AKARI/IRC PSC calibration might not represent a statistically significant sample, also in view of the rather poor coverage at low flux levels.

To assess the completeness of the AKARI-MIR survey we have thus taken a different approach, based on the distribution of sources according to their flux. Figure 17 shows the histogram of AKARI MIR sources in the S9W and L18W bands with a similar histogram for the IRAS PSC sources. This histograms show an interesting feature: source counts decline exponentially after a peak value is reached around 0.1 Jy (S9W) and 0.2 Jy (L18W). This is better seen in Figure 18, where the following regressions lines have been over plotted to the data:

$$\log(N) = 2.90 - 1.93 \log(\mathrm{Flux09})$$

$$\log(N) = 2.57 - 1.83 \log(\mathrm{Flux18})$$

One can thus make the reasonable assumption that the exponential decay is an intrinsic property of source counts at the relevant wavelengths and, on this basis, one can define completeness as the ratio of the number of sources actually observed by the number of sources predicted by the above equations. The results of completeness are shown in Figure 19. From this figure we deduce the completeness rations reported in Table 7.

Table 7: Completeness and Signal-to-Noise ratio

	S9W			
Completeness	5%	50%	80%	100%
Flux[Jy]	0.07	0.10	0.11	0.15
S/N	6.7	7.6	8.5	9.8
	L18W			
Completeness	5%	50%	80%	100%
Flux[Jy]	0.10	0.16	0.21	0.28
S/N	5.0	6.5	7.6	8.7

To evaluate the detection limit of the survey, we can make use of the AKARI/IRC PSC Signal-to-Noise characteristics shown in Figure 15. From this figure one can deduce that, for $S/N \sim 5$, the detection limit is about 0.05 and 0.09 Jy in the S9W and L18W bands, respectively.

A summary of the completeness of the survey at various flux levels, together with the corresponding values of the Signal-to-Noise ratio are given in the Table 7. These results are in fairly good agreement with Ishihara et al. (2006, 2008).

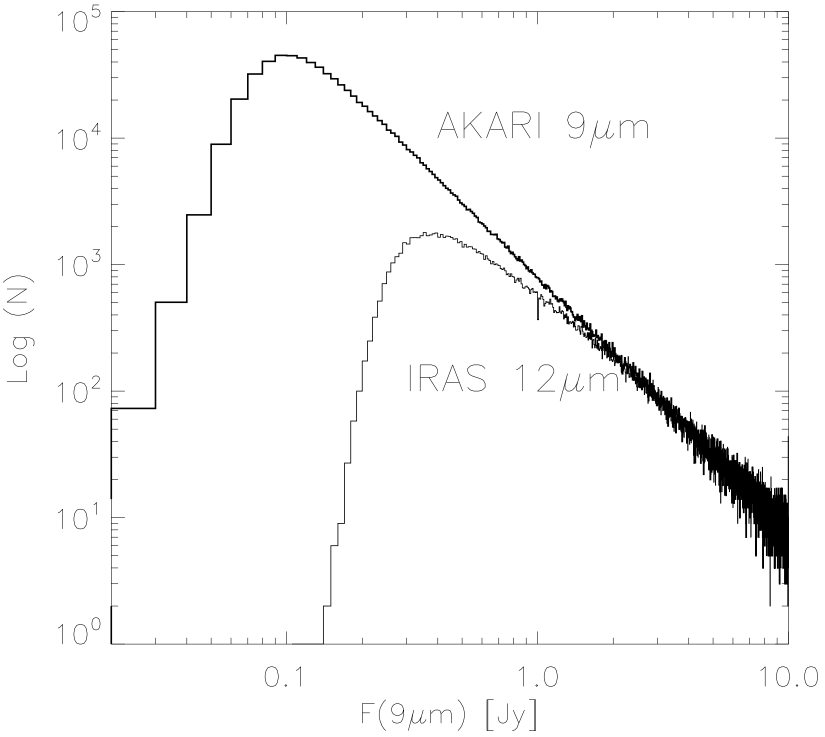

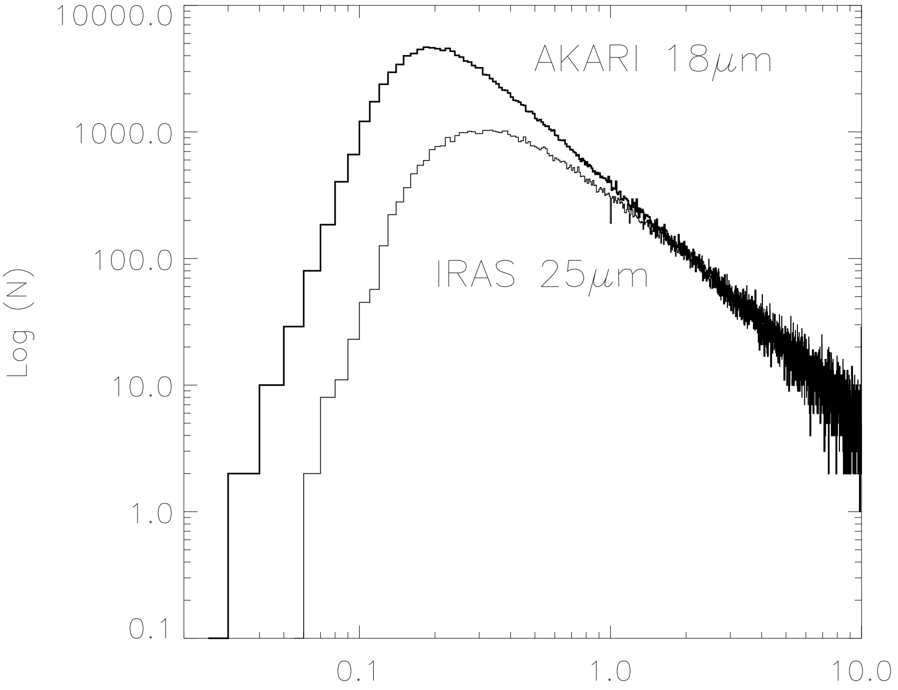

Figure 17: The distribution of sources as a function of the S9W and L18W flux for AKARI/IRC PSC is compared with that from the IRAS survey at 12 μm and 25 μm in log-log scale.

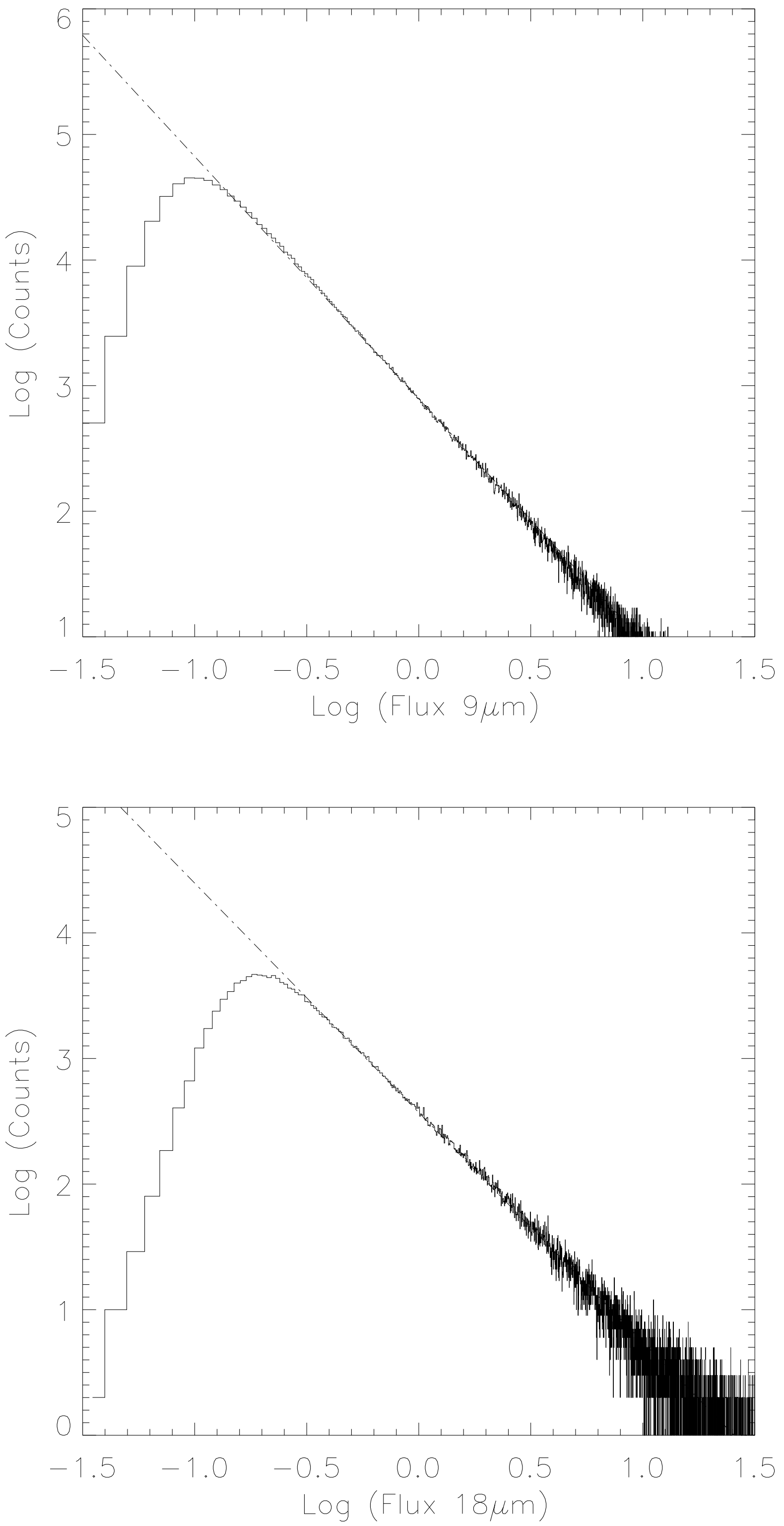

Figure 18: The distribution of sources as a function of the S9W and L18W flux for AKARI/IRC PSC. The over plotted dash-dotted line is a fit to the source counts for fluxes above the peak of the distribution.

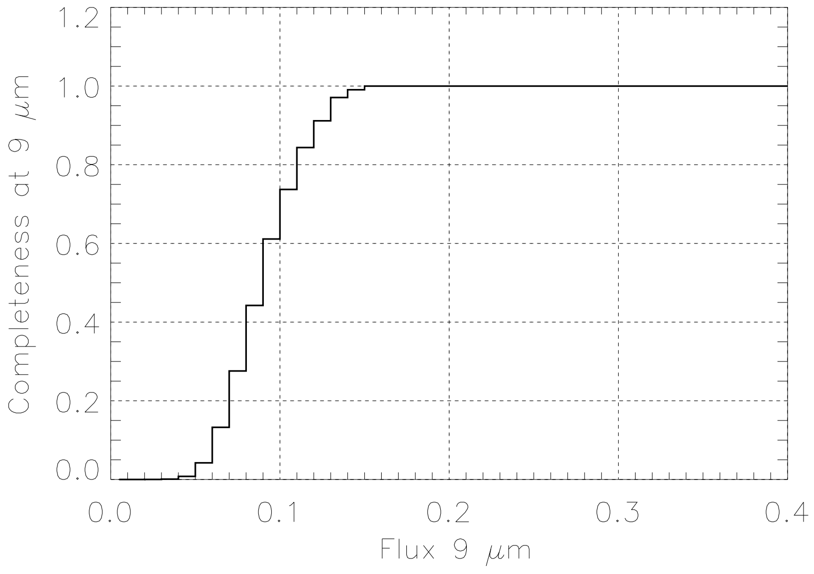

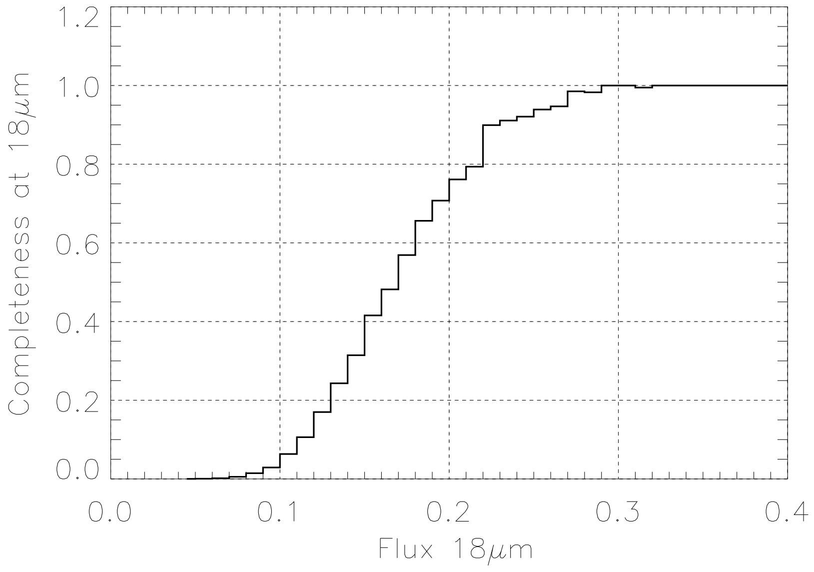

Figure 19: Completeness ratio of the AKARI/IRC survey in the S9W and L18W bands.

REFERENCES

Bertin, E., and Arnouts, S., 1996 A&AS 317, 393
Bertin, E. SExtractor v 2.5 User's manual
Cohen, M., et al. 1992 AJ, 104, 1650
Cohen, M., et al. 1995 AJ, 110, 275
Cohen, M., et al. 1996 AJ, 112, 2274
Cohen, M., et al. 1999 AJ 117, 1864
Cohen, M., et al. 2003a AJ, 125, 2645
Cohen, M., et al. 2003b AJ, 126, 1090
Cohen, M. 2003 in Proc. The Calibration Legacy to the ISO Mission, ESA SP-481, 135
IAU Recommendations for Nomenclaturer, Version 2006 November 28, *http://cdsweb.u-strasbg.fr/iau-spec.html*
Ishihara, D., et al., 2006 PASP 118, 324
Ishihara, D., et al., 2008 SPIE 7010, 70100B-1
Kawada, M., et al., 2007 PASJ 59, S389
Lorente, R., et al. AKARI IRC Data User Manual version 1.4 2008
Murakami, H., et al., 2007 PASJ 59, S369
Onaka, T., et al., 2007 PASJ 59, S401
Tanabé, T., et al., 2008 PASJ 60, S375